

METHODS FOR ANALYTIC REFLECTED RADIANT FLUX MODELING IN OBSERVING SPACE VEHICLES

Kevin R. Kobylka* and Derek A. Hutton†

During NASA's Artemis I mission, the Orion Optical Navigation (OpNav) camera was used in a flight test to capture images of the Interim Cryogenic Propulsion Stage (ICPS) at long range. Novel methods in reflectance modeling were developed to estimate the reflected light flux as a function of range to inform the camera settings used to obtain the images. Postflight analysis was performed with the obtained images and telemetry. Techniques were developed using a specialized tool developed from COTS star identification and attitude determination software to localize ICPS and positively identify it. The images were then used to verify the preflight prediction of reflected radiant flux as a function of range and to provide insight into the vehicles attitude dynamics.

INTRODUCTION

Surface reflectance modeling is a well studied field with many applications in space exploration.^{1,2} It has been used extensively in applications ranging from spacecraft navigation, planetary science and the study of celestial objects, and the estimation of attitude dynamics.^{3,4,5,6,7,8,9} While much of the study has been focused on modeling the light reflected by celestial bodies, less consideration has been given to applying these methods to make similar computations when observing human made spacecraft used in crewed spaceflight operations. Owing to the reduced cost and power benefits of passive optical sensors, and the recent advances in computer vision techniques, use of passive sensors on exploration missions will continue to grow rapidly.^{10,11} Future crewed missions beyond low Earth orbit will require the use of multiple vehicles and multiple Rendezvous Proximity Operations and Docking (RPOD) operations as part of the mission framework. In NASA's planned Artemis missions, passive optical sensors will be critical components in conducting RPOD, therefore developing and extending techniques which improve image-based navigation capabilities will benefit these and future missions.¹²

Developing methods to model the expected brightness of human-made objects is critical to understanding detection ranges for relative bearing measurements during vehicle rendezvous operations. This information is needed to aid in planning missions involving RPOD. Two different analytic models for reflected brightness were developed and are presented here. Data from an Artemis I flight test of the Optical Navigation (OpNav) camera was used to validate and refine the models which will be used for planning on Artemis II and future missions.

BACKGROUND

The Orion spacecraft uses optical sensors for absolute navigation, featuring both star trackers for determining vehicle attitude, and an optical navigation camera which uses imagery of the Earth

*Aerospace Engineer, NASA JSC

†Sr. Staff Software Engineer, Lockheed Martin Space

and Moon for determining absolute attitude and position.¹² Future missions will feature a docking camera which will be mounted looking along the docking axis, to aid in crew situational awareness at close range, and to generate bearing measurements to a rendezvous target vehicle at long range.

While docking will not occur until Artemis III and the first docking camera will not fly until Artemis II, Artemis I featured a flight test to gather data on long range bearing to another vehicle using the Interim Cryogenic Propulsion Stage (ICPS) as an imaging target for the OpNav camera after ICPS had separated from the Orion spacecraft. While the docking camera and OpNav camera are different systems with different mission objectives, certain hardware similarities (such as sensor resolution and Field of View (FOV)) enabled this imagery to be an acceptable surrogate for a long range bearing test comparable in performance to what is expected of the docking camera.

After Orion separated from the ICPS, the OpNav camera captured imagery of the ICPS at a range of approximately 2600 nautical miles. Multiple images were obtained with several seconds between images. The camera exposure time was set to one second based on the preflight reflectance analysis discussed in more detail in the next section. The images obtained were then processed with specialized algorithms to locate ICPS.

PREDICTED BRIGHTNESS AS A FUNCTION OF RANGE

Prior to Artemis I, two different methods were developed to predict the apparent magnitude of ICPS as a function of range when viewed from Orion. One method used simple geometric shapes to model the ICPS and the other used an equivalent flat surface area. These were used to inform the camera exposure time prior to the flight. These are the same models being used to predict target vehicle brightness on Artemis III and beyond, so their application here serves as a test of their readiness for implementation in future flights. An image of the ICPS used on Artemis I is shown in Figure 1.

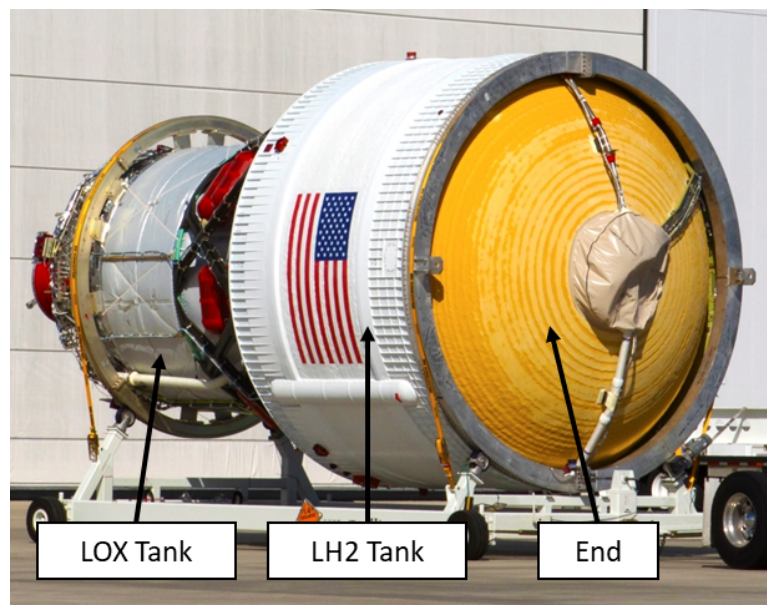


Figure 1 Picture of ICPS with structures used in flat surface radiometry model identified. Credit: NASA

Analytic Brightness from Simplified Geometric Models

At great distances, an object's complex geometry can be approximated by simple shapes (e.g. sphere/cylinder/tri-axial ellipsoid) and the reflectance of the surface represented by a uniform Bidirectional Reflectance Distribution Function (BRDF). This enables the derivation of analytic solutions for total reflected brightness and Centroid of Illumination (COI). These analytic expressions can then provide information beneficial to processing optical measurements of the observed object from a distance.

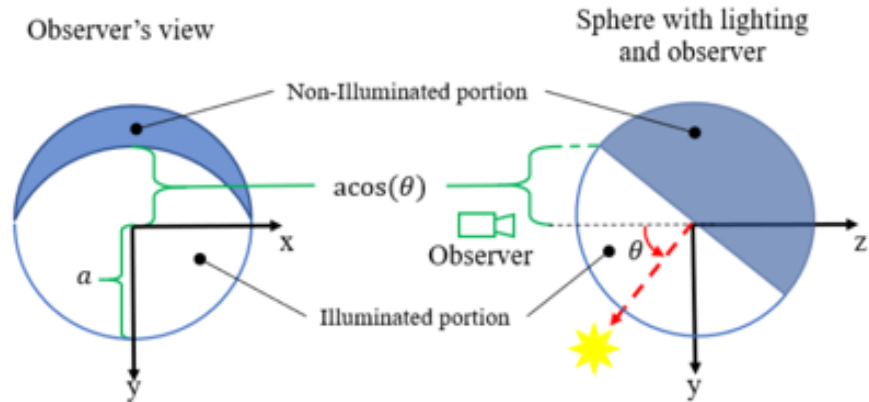


Figure 2 Parameterization of the observation and collimated lighting direction of a simple sphere for derivation of a total reflected brightness equation.

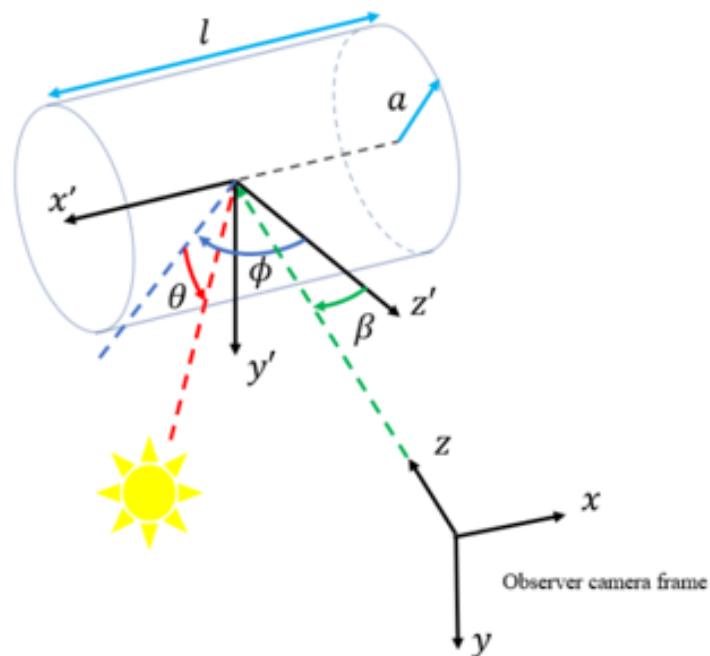


Figure 3 Parameterization of the observation and collimated lighting direction of a simple cylinder for derivation of a total reflected brightness equation.

These methods have been applied extensively in recent decades in improving optical measurements made with respect to other celestial objects which are generally well approximated with a spherical model.^{4,13} More recently, a solution to the cylindrical model (both total brightness and COI) has been derived with several lighting models to facilitate the extension of these methods with respect to human made spacecraft.² The total reflected brightness solutions discussed here have been derived in prior work along with solutions corresponding to other lighting models.^{1,14,2} Figure 2 shows how the analysis parameterizes the sphere, and Figure 3 shows how the cylinder is parameterized. Below is a list of parameters to be used in the analysis:

- I_0 : Irradiant intensity of incident light (in this case sunlight) on the surface W/m² or Ph/m²/s
- α : Albedo – fraction of incident light reflected by surface
- a, l : Geometric (radius and length, respectively) dimensions of object
- \bar{I} : Total reflected brightness
- θ, ϕ, β : Angles describing the incoming lighting direction

Beginning with the sphere, the brightness as a function of x and y on the plane projected along the observers viewing direction (shown in Figure 2) using a Lambertian model is expressed as:

$$I(x, y)_L^s = I_0 \alpha \left[y \sin(\theta) + \sqrt{1 - x^2 - y^2} \cos \theta \right] \quad (1)$$

Integrating Eq. 1 over the projected illuminated area in the x and y directions leads to the following expression for total reflected brightness:

$$\bar{I}_L^S = \frac{2}{3} I_0 \alpha a^2 \left[\sin(\theta) + \cos(\theta)(\pi - \theta) \right] \quad (2)$$

In the cylinder case, using the parameters shown in Figure 3, we can define a similar equation for reflected brightness as a function of position in the x/y plane. Note that because of the uniformity along the cylinder body in the x direction, we need only describe the reflectance as a function in the y direction:

$$I(y)_L^C = I_0 \alpha \left[\sqrt{1 - y^2} \cos(\phi) \cos(\theta) + y \sin(\theta) \right] \quad (3)$$

Integrating over the projected illuminated surface area (as with the sphere), we have:

$$\bar{I}_L^C = \frac{I_0 \alpha a l \cos(\beta)}{2} \left[\cos^2(\theta) \cos(\phi) \sin(\theta) + \cos(\theta) \cos(\phi)(\pi - \theta) + \sin^3(\theta) \right] \quad (4)$$

One can then determine the irradiance received by an observer as a function of the inverse square of the range. One important point for cylindrical objects is that the reflected brightness is very much dependent on the relative attitude of the object being observed. In order to apply these equations, ICPS was approximated as a cylinder in the side-on view case, and as a sphere in the end-on viewing case when only the top of the upper tank is visible. This yielded a high and a low estimate to what might be observed.

Another consideration is the albedo α of ICPS. This quantity represents the fraction of incident light reflected by a differential element of surface area. In order to have an analytic total brightness solution, the albedo is approximated as constant over the visible surface. In this application, the model is assumed to be monochromatic with α varying between 0 and 1, with 0 representing a completely black surface and 1 representing a completely white surface. Approximate values were chosen corresponding to the coloring of the side and top of the ICPS.

The total irradiant flux received by an observer can be calculated as a function of range and be used to determine apparent magnitude as discussed in the section titled Converting Irradiance into Apparent Magnitude. Figure 4 shows the estimated apparent magnitude of ICPS at different phase angles in the side-on and end-on relative attitude. These estimates were initially verified by comparing them with apparent magnitude estimates obtained from an online database, and with the other analysis presented in this work.¹⁵

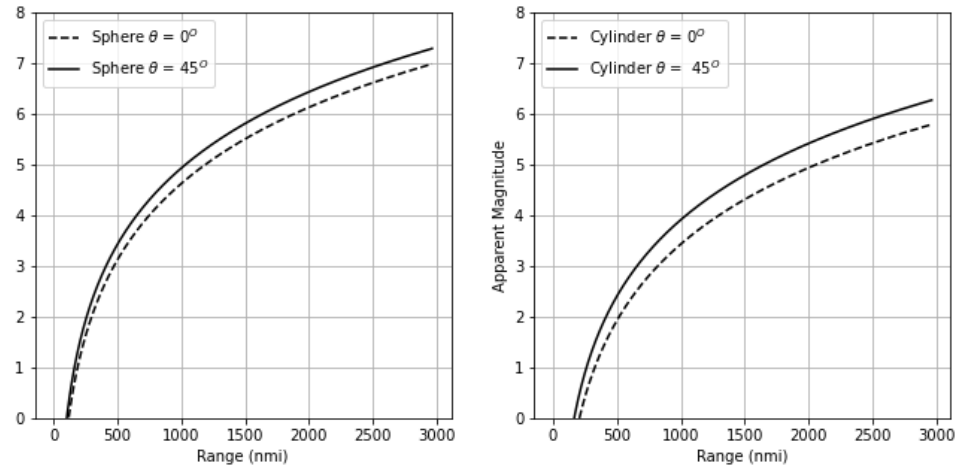


Figure 4 Apparent Magnitude curves as a function of range for an end-on view (*left*) and on a side-on view of ICPS (*right*) estimated using the total brightness equations derived from simplified geometry using a Lambertian reflectance model.

Analytic Brightness from Flat Surface Model

Prior to developing the more detailed geometric reflected brightness model described above, a simplified flat surface model was used to aid in mission planning by estimating the feasibility of detecting the ICPS with the OpNav camera. Similar to the geometric analysis, the flat surface model considered the ICPS in two main viewing orientations: end-on and side-on. However, instead of modeling the geometry of the ICPS as a sphere and a cylinder, the flat surface model simplified the calculations by using an estimated equivalent flat Lambertian surface for each viewing orientation.

Figure 5 depicts the configuration analyzed in the flat surface model and indicates the nomenclature used in the analysis.

Below is a list of parameters used in the flat surface analysis:

- L_{sun}, L_i : Radiance leaving the Sun and ICPS surface, respectively, in $\text{W/m}^2/\text{sr}$
- E_i, E_c : Irradiance incident on the ICPS surface and camera, respectively, in W/m^2

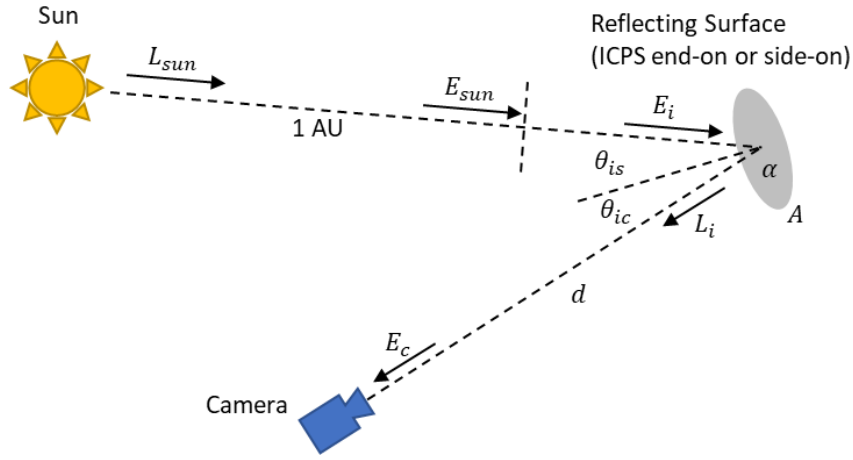


Figure 5 Depiction of the flat surface model configuration.

- E_{sun} : Solar irradiance on a surface whose normal points to the Sun at 1 AU distance, in W/m^2
- α : Albedo – fraction of incident light reflected by the surface
- A : Area of the reflecting surface
- d : Distance from reflecting surface to the camera
- θ_{is}, θ_{ic} : Angles from the ICPS surface normal to the Sun and camera, respectively

Since the ICPS is modeled as a flat Lambertian surface, and the distance d is much greater than the reflecting surface area A , the irradiance received by the camera is given by:¹⁶

$$E_c = L_i \frac{A \cos \theta_{ic}}{d^2} \quad (5)$$

Where L_i is the radiance leaving the reflecting surface and θ_{ic} is the angle between the reflecting surface normal and the surface-to-camera vector.

Since the reflecting surface is assumed Lambertian, L_i can be written in terms of the incident irradiance E_i and the albedo α of the surface:^{16,17}

$$L_i = \frac{\alpha}{\pi} E_i = \frac{\alpha}{\pi} E_{sun} \cos \theta_{is} \quad (6)$$

Where E_{sun} is the solar irradiance on a plane which is perpendicular to the direction to the Sun and θ_{is} is the angle between the surface normal and the direction to the Sun.

Substituting Eq. (6) into Eq. (5) the irradiance received by the camera E_c is:

$$E_c = \frac{\alpha}{\pi} E_{sun} \cos \theta_{is} \frac{A}{d^2} \cos \theta_{ic} \quad (7)$$

At Earth distance, the Sun subtends a right circular cone with half angle Θ_{sun} equal to 26 arcsec and the solar irradiance can be expressed as:¹⁶

$$E_{sun} = L_{sun} 4\pi \sin^2 \left(\frac{\Theta_{sun}}{2} \right) \quad (8)$$

Where L_{sun} is the in-band radiance of the Sun obtained by integrating Planck's radiation law¹⁸ over the waveband of the camera and using a blackbody temperature of 5900 K.

Using Eq. (7), the irradiance from the ICPS for different viewing angles can be estimated if we have values for A and α for the equivalent flat surface. Publicly available photos and dimensions were used to estimate the size and albedo of the ICPS and to estimate an equivalent flat surface model.^{19,20,21,22} One such photo of the ICPS is shown in Figure 1.

The flat surface model assumes that the end-on view sees only the orange surface on the end of the Liquid Hydrogen (LH2) tank, and since the radius of curvature of the tank appears to be significantly larger than the radius of the ICPS, it is modeled as a flat circle with area A_{end} using the radius of the ICPS. The end-on view of the main engine was not considered in the analysis due to the lack of publicly available information.

The side-on view is modeled using only the two primary cylinder structures, the smaller silver cylinder of the LOX tank and the larger white cylinder of the LH2 tank. The equivalent area for each cylinder, A_{lox} and A_{lh2} , was estimated as the length multiplied by the diameter and was scaled by 0.5 to account for the reduced reflected light due to the curved surface.

To estimate the albedo for the different surfaces, the albedo of the white paint on the LH2 tank α_{lh2} was assumed based on common albedo values for white paint. The albedo for the orange coating on the end of the LH2 tank and the silver coating on the LOX tank was estimated by using the photograph in Figure 1 and comparing the brightness of each with the assumed value for the white paint. While the orange coating appears to be diffuse, the silver coating appears to be somewhat specular, therefore the LOX tank albedo was scaled by 0.5 to estimate the diffuse-only component needed in the analysis.

Since albedo and area combine linearly in the radiometry calculations, it is possible to compute a single equivalent flat surface model for the side-on view by combining the two cylinders. This is done by picking a fixed albedo, in this case α_{lh2} , and scaling the area of the LOX cylinder, assuming it has the same fixed albedo, to get an adjusted area A'_{lox} :

$$A'_{lox} = \frac{A_{lox} \alpha_{lox}}{\alpha_{lh2}} \quad (9)$$

Adding the two areas, A_{lh2} and A'_{lox} , and using the fixed albedo, gives the area and albedo values for the ICPS when viewed side-on of $A_{side} = A_{lh2} + A'_{lox}$ and $\alpha_{side} = \alpha_{lh2}$.

Using either the end-on or side-on values computed above for A and α in Eq. (7) allows the estimation of the ICPS irradiance for different ranges and viewing angles. Figure 6 shows the expected brightness of the ICPS in units of apparent star magnitude using the conversion as described in the section titled Converting Irradiance into Apparent Magnitude. The brightness values shown assume the end-on or side-on surface of the ICPS is normal to the camera so $\theta_{ic} = 0$. Curves for different Sun illumination angles θ_{is} are shown.

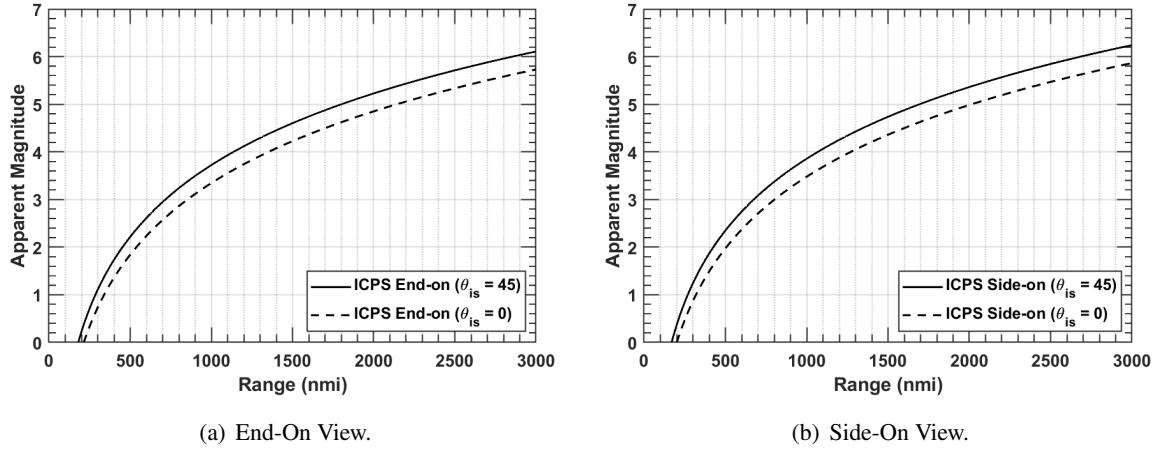


Figure 6 Apparent star magnitude of ICPS reflections using the flat surface model for end-on and side-on views of the ICPS.

Converting Irradiance into Apparent Magnitude

The calculated irradiance of ICPS can be expressed in terms of visual star magnitude which allows an understanding of how bright the ICPS is expected to be relative to stars in the camera's field of view. This information was used to aid the search for ICPS during postprocessing of the images by limiting the star magnitudes needed in the star catalog used in the search.

To convert the ICPS irradiance E to an apparent star magnitude m , the following equation can be used:^{23,24}

$$m = m_0 - 2.5 \log \left(\frac{E}{E_0} \right) \quad (10)$$

Where m_0 and E_0 represent apparent magnitude and irradiance of a reference star. Typically Vega is used as a reference star but the Sun may also be used with values of $m_0 = -26.74$ and $E_0 = E_{sun}$ from Eq. (8).^{25,24}

MISSION DATA AND INITIAL ANALYSIS

During Artemis I, several dozen images were obtained as part of a developmental flight test when ICPS was ~ 2600 nautical miles from Orion. The goal was to analyze the data to both identify ICPS and estimate its brightness in terms of star magnitude to verify the preflight modeling. Both pre-flight analyses estimated an apparent magnitude of approximately 6.0 at this range, putting ICPS on the edge of detectability with the OpNav camera. After the flight, the images were analyzed using a specialized tool developed from a COTS star ID and attitude determination software which referenced the Hipparcos star catalog.^{26,27} Two versions of the Hipparcos catalog were used. The first version included stars of apparent magnitude of 5.5 and brighter and was used for image attitude determination. The second version included stars of magnitude 7.5 and brighter, and was used to reproject all possible star locations and filter out detected centroids occupying those image coordinates. The remaining centroids detected, but not associated with star locations, were then tracked over the course of the images.

We obtained propagated trajectory data for ICPS from the Artemis I Flight Dynamics team and were able to use that in conjunction with Orion's trajectory to determine the projected ICPS image coordinates using the following technique. Supposing a common Earth centered inertial frame, we notate the ICPS position vector as \mathbf{r}_{ICPS} and the Orion position vector as \mathbf{r}_O . The Line-Of-Sight (LOS) vector from Orion to ICPS can then be computed as:

$$\mathbf{e}_{ICPS} = \frac{(\mathbf{r}_{ICPS} - \mathbf{r}_O)}{\|(\mathbf{r}_{ICPS} - \mathbf{r}_O)\|} \quad (11)$$

The transformation from the ICRF frame to OpNav camera frame (based on Orion's known attitude in the ICRF at the time the images were gathered) is described by \mathbf{T}_{ON}^{ICRF} . Using this we can then re-express the ICPS direction vector \mathbf{e}_{ICPS} in the OpNav camera frame \mathbf{e}'_{ICPS} :

$$\mathbf{e}'_{ICPS} = \mathbf{T}_{ON}^{ICRF} \mathbf{e}_{ICPS} \quad (12)$$

Using the OpNav camera calibration matrix \mathbf{K} , we can then compute the rough pixel coordinates of ICPS as:

$$\mathbf{u}_{ICPS} = \mathbf{K} \mathbf{e}'_{ICPS} \quad (13)$$

Computing the ICPS image coordinates over the course of the obtained images indicated that the calculated direction to ICPS changed very little, meaning that we should expect it to be stationary with respect to the starfield.

Image Processing

While we now possess an idea of where ICPS is in the image, it is important to note that we did not consider uncertainties in either vehicles' computed position estimate, or distortion parameters in the camera. In light of this, we chose a small search area around the predicted ICPS image coordinates to begin our search. Within this region, a centroid was detected consistently in the same location, albeit only picked up intermittently by the star centroiding algorithm. Given that ICPS was expected to be extremely dim, a secondary centroid search was performed within the chosen region using lower thresholds for pixel intensity and centroid size, which effectively lowers the criteria for a signal to be detected as a possible centroid. This lowered threshold was only applied to the small search area since applying it to the entire image resulted in a prohibitive number of spurious returns. The lowered threshold resulted in a centroid appearing consistently across the set of images in the predicted location. These steps are shown in Figures and .

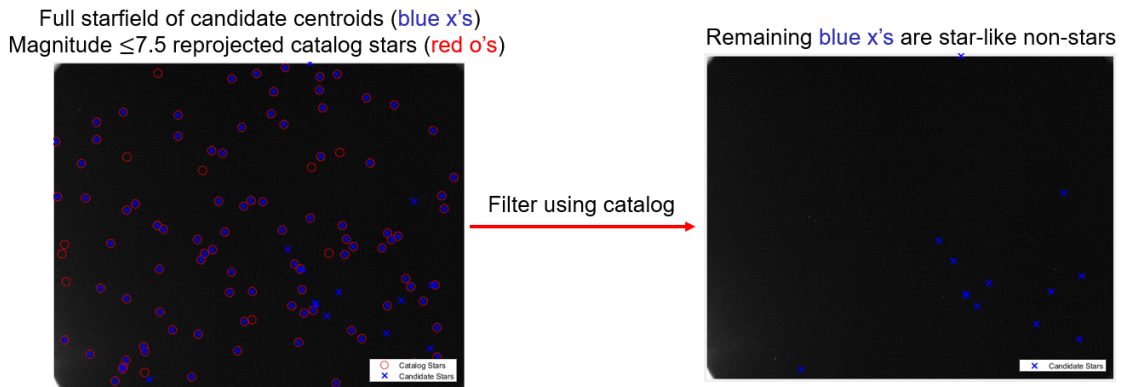


Figure 7 Stars from a 7.5 magnitude thresholded catalog were reprojected onto the images to filter out all the centroids that were indeed stars, leaving us with non-star centroids which are the ICPS candidates.

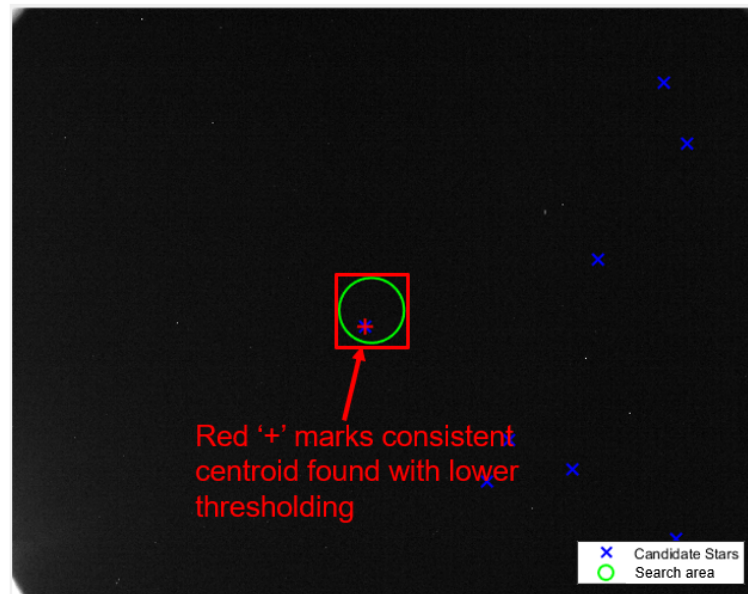


Figure 8 The green circle represents the smaller search area around the unit direction generated from the propagated telemetry data. The blue x represents ICPS being found by the main whole-image centroid finding algorithm, while the red + represents the centroid as found by the windowed, low threshold search algorithm.

Given that ICPS was expected to remain in approximately the same location in the image, the windowed portions of the image (where the lowered thresholding search was conducted) were then stacked. This amplified signals that were stationary across images allowing very dim signals to become visible. This process yielded a very strong return in the region of interest, consistent where ICPS was expected to be as shown in Figure 9.

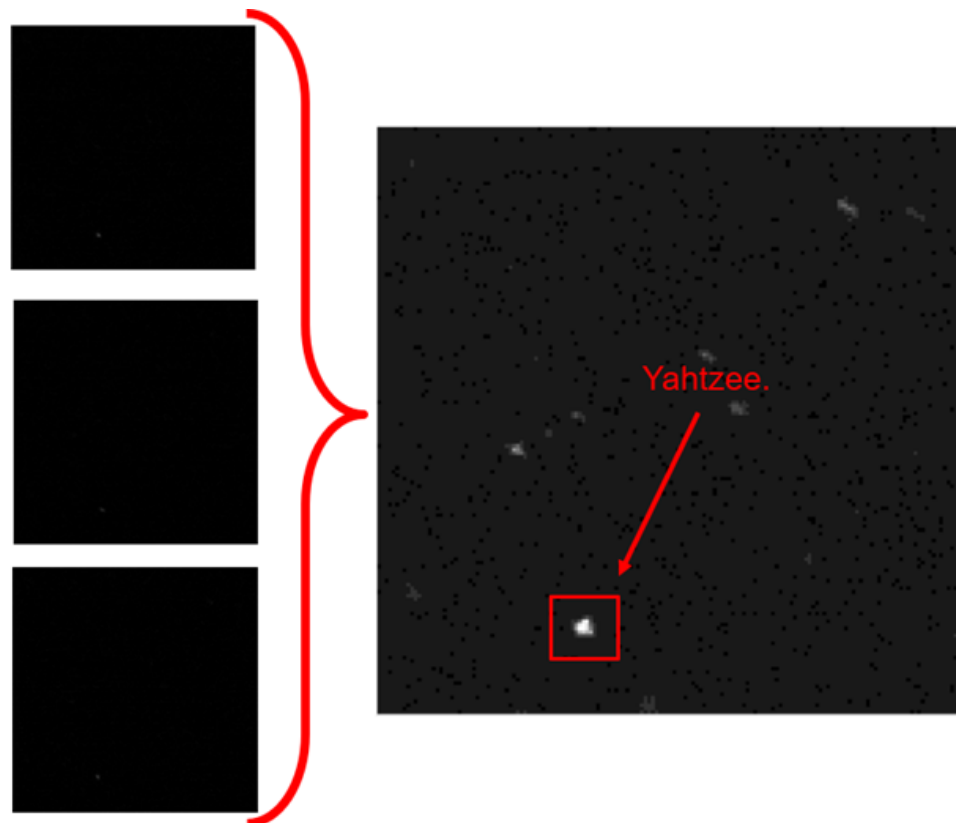


Figure 9 By stacking the windowed images from the ICPS search area, we can amplify the dim signal to see a consistent return.

Brightness Model verification In order to determine a rough verification of the brightness models derived in the earlier sections, the average peak pixel intensity of the ICPS centroid was compared with that of the stars in the image. The peak pixel intensity of all the stars detected in the image set was averaged across matching apparent magnitude values to define a relationship between average peak pixel intensity and stellar apparent magnitude. The fitted logarithmic curve was used to determine the ICPS apparent magnitude based on the average peak intensity of the ICPS centroid, shown in Figure 10. The computed value aligned well with the predicted values from preflight analyses.

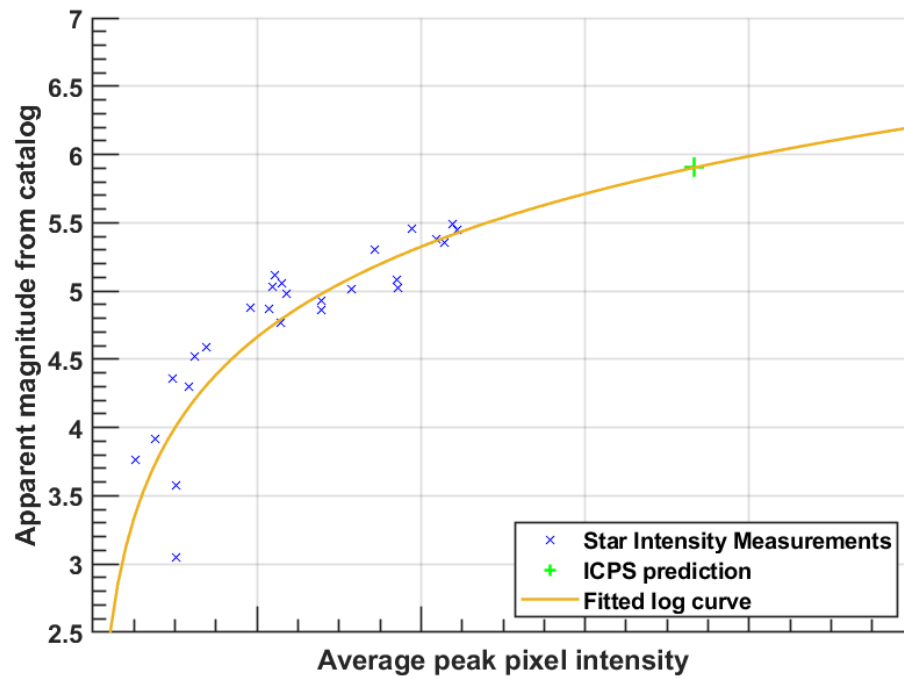


Figure 10 A relationship was determined between stellar apparent magnitude and average peak pixel intensity for identified stars. The resulting trend was used to estimate ICPS's apparent magnitude based on its average peak pixel intensity, confirming the preflight estimates made using analytical models.

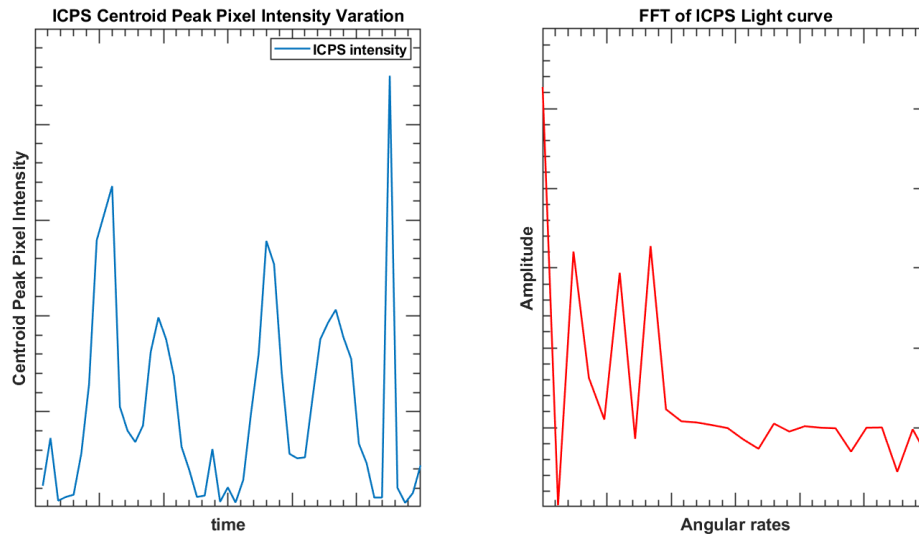


Figure 11 The peak pixel intensities of the ICPS centroid over the duration of the images gathered (*left*) and the Fourier transform of the ICPS max centroid intensity over the duration of the images (*right*) shows spikes at a few angular rates, which were confirmed to be plausible based on the mass properties of the vehicle and its post separation attitude profile.

Angular rates The peak pixel intensity for the ICPS centroid in the image varied with a distinctive pattern over the course of the images gathered, shown in Figure 11. This type of signature, characterized by the combination of low and high frequency signals over time, is commonly seen in the brightness curves of tumbling, oblong objects. Brightness curves can be used in a process called light curve inversion whereby the angular rates of a tumble can be estimated by taking the Fourier transform of the observed signal.^{8,28,29,30,9} With only one observer, only the normed angular rates can be estimated – determining the specifics of the tumble to higher fidelity would require simultaneous observations from different observers to be combined. In the case of the ICPS, the Fourier transform of the time varying intensity signal is shown in Figure 11. While the specific values cannot be released, the angular rates shown in the Fourier transform were confirmed to be roughly commensurate with the mass properties of the vehicle and the post separation maneuvers conducted.

CONCLUSION

A flight test on Artemis I was conducted to evaluate the observability of another human-made spacecraft at long range using a visual band imaging system to investigate the use of such systems in generating long range bearing measurements on future missions. The test entailed using Orion's optical navigation camera to gather imagery of the Interim Cryogenic Propulsion Stage (ICPS) after separation, when ICPS was at a range of approximately 2600 nautical miles. Preflight analyses were conducted to estimate the brightness as a function of range of a human made object with cylindrical and spherical geometric elements. These estimates informed camera settings during the flight test, and the expected brightness of ICPS in the images.

Once the data were gathered, a specialized tool was developed using a COTS star ID and attitude determination tool as the base to filter the images for very dim signatures, with a windowing function and secondary thresholding feature added to search for dim signatures in a smaller region of the images. Trajectory information from the Artemis I Flight Dynamics group was then used to localize the search area in the image and a signature matching ICPS's estimated location and motion was identified and confirmed using an image stacking technique to amplify the signal. The pixel intensities and known apparent magnitudes of identified stars in the image set were then used to establish a correlation between intensity and apparent magnitude. This correlation was used to verify the estimated ICPS apparent magnitude calculated in the preflight analyses. Finally, a pattern was observed in the ICPS intensity which resembled that of a tumbling oblong object, and was used to estimate the approximate angular rates of the tumble, which was commensurate with the known mass properties and attitude maneuvers conducted by the vehicle.

In closing, analytic reflectance models which are commonly used in applications related to the observation of celestial objects were successfully extended to determine the approximate apparent magnitude of a distant, human made spacecraft. The data gathered during the Artemis I flight not only demonstrated the viability of using an optical system for obtaining bearing measurements, but also demonstrated its viability at long range with the inclusion of a priori knowledge and image processing techniques. It was also demonstrated that the same imagery can be used to estimate the attitude rates of a tumbling spacecraft. The results of this flight test demonstrate a strong future for optical imaging systems, image processing techniques, and analytic reflectance modeling within the realm of onboard relative navigation to other human made vehicles.

ACKNOWLEDGMENT

The authors would like to thank Phil Gatt and Brad Smith at Lockheed Martin for their consultation and advice on radiometry topics.

REFERENCES

- [1] K. R. Kobylka, *Photometric and geometric methods for enhanced image-based spacecraft navigation*. PhD thesis, Rensselaer Polytechnic Institute, 2021.
- [2] K. R. Kobylka, J. H. Puritz, and J. A. Christian, "Analytic Center Of Illumination Solutions to Aid Relative Navigation with Partially Resolved Imagery," *2019 AAS/AIAA Astrodynamics Specialist Conference*, 2019.
- [3] C. A. Wright, A. J. Lionus, and B. W. Ashman, "Optical Navigation Algorithm Performance," *1st Annual RPI Workshop on Image-Based Modeling and Navigation for Space Applications*, 2018.
- [4] K. Muinonen and K. Lumme, "Disk-Integrated Brightness of a Lommel-Seeliger Scattering Ellipsoidal Asteroid," *Astronomy & Astrophysics*, Vol. 584, No. A23, 2015.
- [5] L. Lindegren, "Meridian observations of planets with a photoelectric multislit micrometer," *Astronomy and Astrophysics*, Vol. 57, 1977, pp. 55–72.
- [6] M. Kaasalainen and P. Tanga, "Photocentre offset in ultraprecise astrometry: Implications for barycentre determination and asteroid modelling," *Astronomy & Astrophysics*, Vol. 416, No. 1, 2004, pp. 367–373.
- [7] B. Hapke, *Theory of reflectance and emittance spectroscopy*. Cambridge university press, 2012.
- [8] S. Fan, A. Friedman, and C. Frueh, "Satellite Shape Recovery from Light Curves with Noise," *Advanced Maui Optical and Space Surveillance Technologies Conference* (S. Ryan, ed.), September 2019, retrieved 1 October 2021.
- [9] S. Fan and C. Frueh, "A Direct Light Curve Inversion Scheme in the Presence of Measurement Noise," *The Journal of the Astronautical Sciences*, Vol. 67, No. 2, 2020, pp. 740–761.
- [10] J. A. Christian, "A Tutorial on Horizon-Based Optical Navigation and Attitude Determination with Space Imaging Systems," *IEEE Access*, Vol. 9, 2021, pp. 19819–19853.
- [11] W. Owen, T. Duxbury, C. Acton, S. Synnott, J. Riedel, and S. Bhaskaran, "A Brief History of Optical Navigation at JPL," *AAS Guidance and Control Conference*, No. AAS 08-053, AAS 08-053, Breckenridge, CO, 2008.

- [12] G. N. Holt, C. N. D'Souza, and D. W. Saley, "Orion Optical Navigation Progress Toward Exploration Mission 1," *2018 Scitech Space Flight Mechanics Meeting*, Kissimmee, FL, 2018.
- [13] K. Muinonen and O. Wilkman, "Spherical Albedo of a Lommel-Seeliger Scattering Ellipsoidal Asteroid," *Proceedings of the International Astronomical Union*, Vol. 10, No. S318, 2015, pp. 206–211.
- [14] K. Muinonen, O. Wilkman, A. Cellino, X. Wang, and Y. Wang, "Asteroid Lightcurve Inversion with Lommel-Seeliger Ellipsoids," *Planetary and Space Science*, Vol. 118, 2015, pp. 227–241.
- [15] C. Peat, "Heavens-Above," <https://www.heavens-above.com/>. Accessed: November 2022.
- [16] J. M. Palmer and B. G. Grant, *The Art of Radiometry*. SPIE Press, 2010.
- [17] W. L. Wolfe, *Introduction to Radiometry*. SPIE Press, 1998.
- [18] E. Charles and Z. Jakob J. van, *Introduction to the Physics and Techniques of Remote Sensing*, Vol. 2nd ed of Wiley Series in Remote Sensing. Wiley-Interscience, 2006.
- [19] ULA, *Delta IV Launch Services User's Guide*. United Launch Alliance, LLC, Centennial, CO 80155, 2013. <https://www.ulalaunch.com/docs/default-source/rockets/delta-iv-user's-guide.pdf>.
- [20] ULA, "Interim Cryogenic Propulsion Stage (ICPS)," [https://www.ulalaunch.com/interim-cryogenic-propulsion-stage-\(icps\)](https://www.ulalaunch.com/interim-cryogenic-propulsion-stage-(icps)).
- [21] NASA, "The Marshall Star," 2017. <https://www.nasa.gov/centers-and-facilities/marshall/the-marshall-star-222/>, Last accessed on 2024-01-02.
- [22] NASA, "Major Assembly Complete on System That Will Pack a Powerful Push for Orion," 2016. <https://www.flickr.com/photos/nasamarshall/31415354110>, Last accessed on 2024-01-02.
- [23] M. A. Seeds and D. E. Backman, *Foundations of Astronomy*, Vol. 4. Wadsworth Publishing Company, 1997.
- [24] J. A. Christian, "StarNAV: autonomous optical navigation of a spacecraft by the relativistic perturbation of starlight," *Sensors*, Vol. 19, No. 19, 2019, p. 4064.
- [25] NASA, "Sun Fact Sheet," 2022. <https://nssdc.gsfc.nasa.gov/planetary/factsheet/sunfact.html>, Last accessed on 2024-01-02.
- [26] M. A. C. Perryman, L. Lindegren, J. Kovalevsky, E. Hoeg, U. Bastian, P. L. Bernacca, M. Cr    , F. Donati, M. Grenon, M. Grewing, F. van Leeuwen, H. van der Marel, F. Mignard, C. A. Murray, R. S. Le Poole, H. Schrijver, C. Turon, F. Arenou, M. Froeschl  , and C. S. Petersen, "The HIPPARCOS Catalogue," *Astronomy and Astrophysics*, Vol. 323, July 1997, pp. L49–L52.
- [27] S. Pedrotty, R. Lovelace, J. Christian, D. Renshaw, and G. Quintero, "DESIGN AND PERFORMANCE OF AN OPEN-SOURCE STAR TRACKER ALGORITHM ON COMMERCIAL OFF-THE-SHELF CAMERAS AND COMPUTERS," 02 2020.
- [28] M. Polo, R. Abay, S. Gehly, A. Lambert, P. Lorrain, S. Balage, M. Brown, and C. Bright, "Attitude Detection of Buccaneer RMM CubeSat through Experimental and Simulated Light Curves in combination with Telemetry Data," *Advanced Maui Optical and Space Surveillance Technologies Conference (AMOS)*, Maui, HI, 2018, retrieved 15 August, 2021.
- [29] A. Wang, X.-B. Wang, K. Muinonen, X. L. Han, and Y.-B. Wang, "Light Curve Inversion of Asteroid (585) Bilkis with Lommel-Seeliger Ellipsoid Method," *Research in Astronomy and Astrophysics*, Vol. 16, No. 12, 2016, p. 180.
- [30] A. Wang, X. Wang, K. Muinonen, and X. L. Han, "Photometric Analysis for the Slow Rotating Asteroid (103) Hera Using Convex Inversion and Lommel-Seeliger Ellipsoid Methods," *Planetary and Space Science*, Vol. 167, 2019, pp. 17–22.